Journal of Materials Chemistry C

ROYAL SOCIETY OF CHEMISTRY

PAPER

View Article Online
View Journal | View Issue

Cite this: J. Mater. Chem. C, 2025, 13, 2956

Synthesis and phase purity of the negative thermal expansion material ZrV_2O_7†

Aistė Miliūtė, [ab] Joana Bustamante, [a] Stephanos Karafiludis, [ab] Moritz Zöllner, [ab] Mustapha Eddah, [a] Franziska Emmerling, [ab] Björn Mieller, *[a] Janine George *[ac] and Tomasz M. Stawski *[a]

Received 25th September 2024,
Accepted 9th December 2024

DOI: 10.1039/d4tc04095c

rsc.li/materials-c

Synthesis of pure, homogeneous, and reproducible materials is key for the comprehensive understanding, design, and tailoring of material properties. In this study, we focus on the synthesis of ZrV_2O_7, a material known for its negative thermal expansion properties. We investigate the influence of solid-state and wet chemistry synthesis methods on the purity and homogeneity of ZrV_2O_7 samples. Our findings indicate that different synthesis methods significantly impact the material's characteristics. The solid-state reaction provided high-purity material through extended milling time and repeated calcination cycles, while the sol–gel reaction enabled a "near-atomic" level of mixing, and therefore, homogenous phase-pure ZrV_2O_7. We confirmed purity *via* X-ray diffraction and Raman spectroscopy, highlighting differences between phase-pure and multiphase ceramics. These analytical techniques allowed us to distinguish subtle differences in the structure of the material. Based on *ab initio* simulated phonon data, we were able to interpret the Raman spectra and visualise Raman active atom vibrations. We show that phase purity enables the unbiased characterisation of material properties such as negative thermal expansion.

Introduction

Ceramic materials with unique thermal expansion properties have attracted considerable interest in recent years due to their potential applications in various fields.[1,2] Among these, zirconium vanadate (ZrV_2O_7) stands out for its remarkable negative thermal expansion (NTE) behaviour over a wide temperature range.[3] This unusual property, in which the material contracts when heated, opens up exciting possibilities for creating composites with tailored thermal expansion properties.

In zirconium vanadate (ZrV_2O_7), a unit cell contracts isotropically with increasing temperature over a range of 130 °C to 800 °C.[3,4] The synthesis of zirconium vanadate ceramics, exhibiting NTE, enables the fabrication of composites where the overall expansion coefficient can be tailored to a specific negative, positive, or neutral value.[5] Consequently, such composite materials are attractive for many device applications because they can compensate for damage caused by thermal expansion. NTE composites are relevant to optical systems, electronic and biomedical applications.[5] Furthermore, ZrV_2O_7 has attracted further interest due to its photocatalytic activity[6] and specific discharge capacity.[7] The photocatalytic activity of ZrV_2O_7 and its substituted analogues has been considered for the degradation of various dyes,[8] in sensors and inorganic ion exchangers.[6] Also, Yb^{3+}/Er^{3+} co-doped ZrV_2O_7 may have potential application in the display technology.[9] The NTE property, which prevents damage from volume expansion, combined with the specific discharge capacity of ZrV_2O_7, makes it a promising cathode material for secondary lithium batteries.[7] However, while ZrV_2O_7 exhibits high specific capacity as a cathode material, its capacity retention could be improved. In this context, this promising electrochemical application and the associated challenges highlight complex dependencies between

[a] Federal Institute for Materials Research and Testing (BAM), Berlin, Germany. E-mail: bjoern.mieller@bam.de, janine.george@bam.de, tomasz.stawski@bam.de
[b] Humboldt Universität zu Berlin, Department of Chemistry, Berlin, Germany
[c] Friedrich Schiller University of Jena, Institute of Solid-State Theory and Optics, Jena, Germany

† Electronic supplementary information (ESI) available: Detailed particle size distribution measurement description and summarized results (Table S1). XRD instrumental parameters and analysis description including phase quantification results, plots, and Rietveld refinement parameter list. Phase quantification data covers solid-state 40′ 5 h sample (Fig. S1), commercially available ZrV_2O_7 (Fig. S2), solid-state 180′ 20 h × 3 (Fig. S3), solid-state 40′ 5 h N2-quenched (Fig. S4), solvothermal reaction product (Fig. S5), sol–gel_160 °C (Fig. S6), sol–gel_100 °C (Fig. S7), sol–gel_RO^- (Fig. S8) and sol–gel_Cl reaction product (Fig. S9). Experimental analysis and computational simulations of Raman spectra, including description and plot of room-temperature spectra fitting (Fig. S10) and parameters used to simulate theoretical positions of Raman active modes. A comparison of calculated and fitted experimental frequencies is shown in Table S2. Visualisations of Raman active phonon vibrations are included for the spectral range of 200 to 1100 cm^{-1} as attached GIF files. Scanning electron microscopy images of solvothermal, sol–gel_Cl and solid state 40′ 20 h × 3 reactions showing the morphology of corresponding samples (Fig. S11). Thermogravimetric analysis (TGA) method description and analysis results. TGA weight loss curves of 40′ milled ZrO_2 and V_2O_5 mixture heated from room temperature to 400 °C and 700 °C, held at that temperature for 20 h and cooled down to room temperature are presented in Fig. S12. See DOI: https://doi.org/10.1039/d4tc04095c

the intrinsic properties of crystal structures and the microstructure of the material. Namely, there is a correlation between crystallite sizes, porosity, and measured capacity retention,[7] demonstrating the need to tune the purity, size, and homogeneity of synthesised particles. The potential applications in which the material must be tuned simultaneously in terms of NTE and other physicochemical properties exemplify the fact that the microstructural qualities of the material are fundamental.

An important part of NTE materials research is related to lowering the offset temperature of linear negative thermal expansion to room temperature. This can be achieved, for example, by partially substituting V with P,[4] Mo[8,10] or W.[11] Or lowering thermal expansion *via* double substitution of Fe/Mo,[12] Cu/P[13] or Nb, Y/P[14] for Zr/V sites. The goal is to tune the phase transition temperature and extend the NTE property to manage the thermal expansion of materials more effectively, especially in devices where dimensional stability is essential at lower temperatures.

Despite the growing number of studies investigating the potential applications of ZrV_2O_7, the existing literature on the synthesis and resulting quality of ZrV_2O_7 ceramics remains inconclusive. Many synthesis methods have been reported throughout the 80 years of research, including single crystal, various solid-state synthesis attempts, and wet-chemistry methods. Currently, our understanding of the physicochemical properties of the material is mainly based on extensive single-crystal studies by Evans *et al.*[15] In this regard, single crystals enable us to evaluate the fundamental crystallographic principles of NTE. However, material characteristics will inevitably differ in the case of bulk polycrystalline powder samples and sintered ceramics. The structural comparison among powders derived through different methods and strategies would be an important milestone towards any larger-scale production attempt.

ZrV_2O_7 is derived by reacting stoichiometric amounts of ZrO_2 and V_2O_5. Thus, at its core, the synthesis challenge is related to the extent of mixing of zirconium and vanadium precursors. The phase diagram suggests that if zirconium and vanadium precursors are not well mixed and remain separated over a more considerable local distance, final local stoichiometry can diverge and lead to the formation of competing phases such as $Zr_3V_3O_x$ (x = 1.0 or 0.6)[16] or residual ZrO_2 and V_2O_5. Analysis of a multi-phase material might lead to misleading results, in which the overall elemental composition would match that of ZrV_2O_7, but other non-NTE crystalline phases would be present. Although it may appear to be a trivial matter, as we discuss further, there is commercially available "zirconium vanadate", which contains, in fact, very little actual ZrV_2O_7. Here, we systematically investigate various synthesis methods, including solid-state, sol–gel, and solvothermal, to determine reliable routes for producing phase-pure ZrV_2O_7.

Janine George

Janine George is a junior research group leader and a Professor of Materials Informatics at the Federal Institute for Materials Research and Testing (BAM) in Berlin and at Friedrich Schiller University in Jena (FSU Jena), Germany. She completed her MSc in Chemistry in 2013 and, in 2017, her doctorate in computational solid-state chemistry at RWTH Aachen University. In 2018, she started her postdoc and, later, Marie-Skłodowska-Curie fellowship at UCLouvain in Belgium. Since 2021 is a junior group leader at BAM and FSU Jena. In 2023, she became a Professor of Materials Informatics in Jena. She was a Falling Walls Finalist for "Breakthrough of the Year" in the "Physical Sciences" in 2021. She received a junior scientist award from the Stiftung Werner-von-Siemens-Ring in 2023. In 2024, she received the ERC Starting Grant. She is using atomistic simulations and machine learning to design material properties. To do so, she is linking quantum-chemical bonding information and material properties.

Experimental section

Synthesis strategy

Solid-state reactions. Solid-state synthesis is attractive thanks to its simplicity and cost-effectiveness, making it ideal for potential upscaling. In this method, well-mixed reagents are heated and maintained at a higher temperature, initiating diffusional exchange among grains of the reagents and leading to structural changes in the material (Fig. 1b). In the case of ZrV_2O_7, we face the challenge of slow reaction kinetics, thus necessitating exceedingly long heating steps. After the direct reaction of zirconium dioxide and vanadium pentoxide, some remnants of ZrO_2 are always detected. Early attempts to purify this material were extremely slow and ineffective with extreme-duration heating up to 1000 h.[17] In 1995, Korthuis *et al.* introduced an alternative solid-state synthesis with two 24-hour calcination cycles of zirconium chloride and ammonium vanadate mixture. This reaction was further used in some reports.[18,19] In the last two decades, even though it was generally known that it could be challenging to form high-purity ZrV_2O_7, regardless, ZrO_2 and V_2O_5 were mainly used as reagents with a heating step time decreasing from ~100 hours[20,21] to as low as 4–8 hours.[9,13,22,23]

It is clear that uniform elemental mixing is crucial to obtaining high-quality products and needs to be improved. Reaction and processing parameters such as milling time and heating cycles with intermediate grinding steps could improve the purity of the final product. We refer to purity as the amounts of reagents remaining in the mixture and other side products limited to the minimum or removed altogether. Milling techniques can reduce particle size, leading to better homogeneity of the reactants and improved reactivity due to a higher surface–volume ratio. Additionally, repeated calcination cycles with intermediate grinding can promote a more thorough mixing of elements, ensuring a more uniform reaction throughout the material. Furthermore, quenching the product

after synthesis can improve its purity by preventing undesired low-temperature processes.

We considered all these approaches within the ZrV_2O_7 system to assess the possible limits and relevant attempts of the solid-state reaction for purity and homogeneity. However, even with perfectly tuned parameters of solid-state synthesis, the extent of mixing within a bulk volume remains limited, and at best, Zr and V are separated from each other over distances of a few tens of nm or more. The presence of the remaining unreacted materials can be established when compared with the phase pure simulated X-ray diffraction (XRD) pattern from the optimised ZrV_2O_7 crystal structure (Fig. 1a). For clarity, a selected representative q range from a broader diffraction pattern will be displayed in the figures, which includes peak positions corresponding to ZrV_2O_7, V_2O_5 and ZrO_2. (See solid state synthesis).

Wet-chemistry methods. As an alternative to solid-state reactions, wet-chemistry methods evade extended heating times and offer improved mixing. Various wet-chemistry methods, such as sol–gel and hydrothermal synthesis,[24] have been reported to be successful at providing ZrV_2O_7. In particular, the sol–gel reaction can ensure improved "near-atomic-scale" mixing. Different publications report similar sol–gel synthesis routes with varying parameters (stirring time, temperature, pH and firing time).[4,6,11,17,25,26] Some also describe the fast solution combustion method.[7,8] Aqueous solutions of zirconium nitrate or zirconyl chloride with ammonium metavanadate were mainly used as reagents, with some publications also describing the addition of pure V_2O_5[27] or its solution in oxalic acid.[28]

We investigated the influence of external reaction parameters on sample purity, including a variation of reagents, solvents, and reaction temperature (Fig. 1b). We followed solvothermal,[29] nonhydrolytic[30] and hydrolytic[31] sol–gel methods for the analysis (Fig. 1b). The main difference between these methods is that the hydrolytic sol–gel method uses water. The hydrolysis and condensation reactions lead to the formation of a sol, which then undergoes further condensation to form a gel. In the nonhydrolytic and solvothermal methods, organic oxygen donors, such as ethers, alcohols, or alkoxides, replace water to supply the oxygen needed for the oxide network formation.[31] In addition, the solvothermal method involves high-pressure and temperature conditions to improve chemical diffusion and reactivity, among others. In principle, the goal of all these wet-chemical approaches is to mix and stabilise Zr and V in the form of "dissolved" species such as ions, clusters, small macromolecules, *etc.*, thus enabling the higher diffusivity and near-atomic level of elemental mixing better than that of solid-state methods.

Nonhydrolytic sol–gel hot injection synthesis was selected to provide a controlled environment for direct elemental reactions through mixing precursors at elevated temperatures. In contrast, hydrolytic sol–gel reactions allow a comparison of how

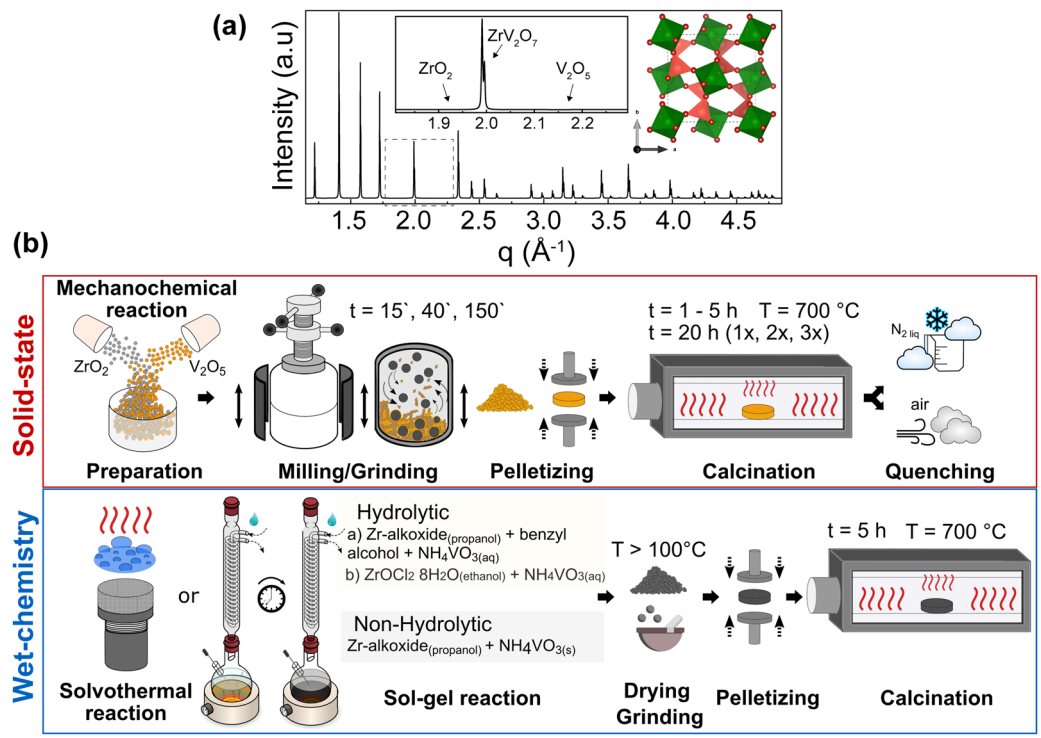

Fig. 1 (a) A simulated X-ray diffraction pattern from ZrV_2O_7 crystal structure. Green polyhedra correspond to ZrO_6 octahedra and dark pink tetrahedra to VO_4. The selected representative area from a broader range is shown as an inset. (b) Overview of solid-state and wet-chemistry reactions. Solid-state method variations include milling times (15′, 40′, and 180′) and calcination for 5 h and 20 h cycles repeated 1, 2, or 3 times at 700 °C. Selected samples were heated for 5 h and quenched in air or liquid nitrogen (b top). Wet-chemistry methods include solvothermal, nonhydrolytic hot injection, and hydrolytic sol–gel reactions (b bottom). Further 2–7 figures include symbols used here to associate results with corresponding synthesis methods and synthesis steps.

the hydrolysis rate influences the purity and homogeneity of ZrV_2O_7. Previous methods and solvothermal reactions increase the sample size and, therefore, the reliability of the results. We also used an already-reported synthesis method (sol–gel_Cl)[26] that allows better insight into already published data and reproducibility attempts. (See solution-based synthesis methods).

The utility of pure samples. The reproducibility of multiphase materials can be challenging if the aimed composition is unknown or deviates from expectations. For example, multiphase materials often cannot be reproduced by following reported incorrectly identified synthesis methods. In addition, if the analysis is performed treating multiphase material as phase-pure, the obtained characterization results would be misleading. Such an issue becomes increasingly complex if, in addition to the ambiguous purity, substitution is considered. This is a concern worth addressing in the NTE research due to growing interest in substituted materials and the fact that NTE property would manifest differently in phase-pure and multiphase materials.

Furthermore, the comparison or validation of results with theoretical methods requires high-quality reference data, which can only be obtained on highly pure and homogeneous samples. For example, predicted (simulated) Raman, IR spectra, or XRD patterns can only be compared with high-quality measured data. Otherwise, excessive peak overlap, data fitting challenges, and difficult-to-resolve structures prevent the reliable comparison and validation of computational results. In particular, the prediction of temperature effects on material properties (*e.g.*, lattice parameter changes with temperature, temperature-dependent vibrational spectra) still poses difficulties for *ab initio* simulations, and methods dealing with anharmonic effects are still under development, so good reference data are particularly important.[32–34] (See Simulated and experimental Raman spectra comparison and Thermal expansion of multi-phase materials).

Materials

Commercially available ZrV_2O_7 was purchased from Onyxmet (CAS-Nr 113981-20-9). The reagents used for the solid-state reactions were zirconium oxide ZrO_2 ($\geq$99%, Carl Roth) and vanadium oxide V_2O_5 (99.9%, Chempur). Analytical grade ZrO_2 and V_2O_5 were additionally dried for 15 h at 100 °C to remove any moisture and to weigh correct stoichiometric amounts. Powders were kept in a desiccator for further use. Particle size distribution of ZrO_2 and V_2O_5 were measured as described in the methods section. Median particle size was $d_{50.3}(ZrO_2)$ = 1.808 μm and $d_{50.3}(V_2O_5)$ = 1.412 μm.

Wet-chemical syntheses were performed using ammonium vanadate NH_4VO_3 ($\geq$99% Sigma-Aldrich) and Zr-alkoxide 70% solution in 1-propanol (Thermo Scientific Chemicals) with benzyl alcohol ($\geq$99.8% Chemsolute). We selected benzyl alcohol as an effective solvent because it can provide monodisperse nanoparticles without adding surfactant[35] and stabilise Zr-alkoxide, which is otherwise sensitive to moisture in the air. Zr-alkoxide also serves as a chloride- and nitrate-free reagent to avoid additional contaminations that are complex to remove during the calcination step. Further information is summarised in the corresponding synthesis sections.

Solid state synthesis

8.08 g of ZrO_2 and 11.9 g of V_2O_5 reagents were mixed at a Zr : V = 1 : 2 molar ratio and ground in a planetary ball mill using plastic containers with 3 mm and 5 mm zirconia balls in ethanol media for 15 min, 40 min, or 3 h (15′, 40′, 180′). The homogenised powder was prepressed at 20 MPa for a few seconds, then pressed at 60 MPa, and dwelt for 1 min. The obtained pellets were 2 cm in diameter and 3 mm in height. Pellets were fired in a tubular furnace at a 5 °C min^{-1} heating rate, held at 700 °C for 1–5 h, 10 h, or 20 h in an ATV PEO 601 annealing furnace, and then cooled naturally to room temperature (RT). Further, calcination for 20 h was repeated two to three times with intermediate grinding in an agate mortar to support a homogenous reaction. Additional air and liquid nitrogen-quenched samples were prepared after 5 h calcination at 700 °C.

Wet chemistry synthesis methods

Solvothermal synthesis. Zirconium vanadate was obtained in a solvothermal reaction at 150 °C after 15 days. The Parr Instrument, 4745 General Purpose Vessel, was used for the reaction. A mixture of ammonium vanadate and Zr-alkoxide 70% solution in propanol was prepared with benzyl alcohol as a solvent.

Nonhydrolytic sol–gel hot injection synthesis (sol–gel_160 °C, sol–gel_100 °C). To carry out this reaction, a 0.2 M 70% solution of Zr-alkoxide in propanol was stabilised with benzyl alcohol and heated to 160 °C (sol–gel_160 °C). Ground NH_4VO_3 was added to the reaction mixture under constant stirring and heated for 4 hours at 160 °C. The collected black slurry was dried overnight at 150 °C. Samples were ground in an agate mortar to obtain powders. The process was repeated, heating up to 100 °C (sol–gel_100 °C).

Hydrolytic sol–gel synthesis (sol–gel_RO^-, sol–gel_Cl). (a) For the sol–gel_RO^- reaction: A 0.2 M Zr-alkoxide 70% solution in propanol was prepared with benzyl alcohol and mixed with an aqueous 0.05 M NH_4VO_3 solution. The mixture was heated at 60 °C for 24 h. After that, the temperature was increased to 100 °C until the water evaporated. The powders were further dried in the air at 180 °C.

(b) For sol–gel_Cl reaction: the samples were prepared as reported by Yanase *et al.*[26] A 0.05 M aqueous NH_4VO_3 solution and a 0.05 M ethanol solution of $ZrOCl_2{\cdot}8H_2O$ (molar ratio Zr : V = 1 : 2) were stirred over 20 h at 60 °C, then dried in the air at 100 °C. Dried samples were ground in an agate mortar to obtain powder samples.

Heat treatment step

All products of the solution-based synthesis methods exhibit amorphous or partially amorphous XRD patterns. Further heating steps that lead to nucleation, growth, and calcination of the zirconium vanadate phase were required. Pellets of 0.5 cm × 0.2 cm (diameter × height) were pressed and heated at 700 °C for 5 h (5 °C min^{-1} heating rate).

Methods

X-ray diffraction (XRD). XRD techniques were used to analyse the structure of ZrV_2O_7 and observe possible additional phases. Various

available techniques were used, including *in situ* X-ray capillary diffraction (XRD), powder diffractions, and synchrotron high-energy diffraction. Phase quantifications using structure refinements were performed with zirconium divanadate (COD (Crystallography Open Database) ID 2002983), zirconium oxide (COD ID 9007485), and divanadium pentoxide (COD ID 9012221). Apart from fitting and phase quantification, the negative thermal expansion property of ZrV_2O_7 allows easy differentiation from residual ZrO_2 and V_2O_5 phases. High-temperature XRD shows different peak shifts with temperature depending on unit cell contraction or expansion. For clarity, a small selection of representative peaks from a broader diffraction pattern will be used in the following figures. See further details on diffraction techniques in the ESI.†

Scanning electron microscopy (SEM). Images of all high-purity samples were collected to analyse homogeneity and microstructure. A Hitachi FlexSEM 1000 scanning electron microscope (SEM) with a W cathode was used for imaging. The samples were investigated in the secondary electron detection mode with the acceleration voltage set to 10 kV and a working distance of 5702.2 μm. The powder was conductive enough to prevent any discharge effects on the carbon tape. Additional images (Fig. 2b) were collected with an SEM/FIB FEI Quanta 3D electron microscope in the secondary electron detection mode, with a 10 kV acceleration voltage and a working distance of 10.0 mm.

Raman spectroscopy. The Raman spectra were acquired using the LabRAM HR800 instrument (Horiba Jobin Yvon) coupled to a BX41 microscope (Olympus) with a 50x (N.A. = 0.55) long working distance objective lens and equipped with a charge-coupled device (CCD) detector (Symphony, Horiba Jobin Yvon). A Nd:YAG laser with an excitation wavelength of 532 nm was used. ND filters were implemented to reduce the maximum laser intensity of 34 mW to 1–10% at the sample surface. All spectra were recorded at room temperature in the spectral range of 180 to 3330 cm^{-1} using both a 300 mm^{-1} grating for lower spectral resolution and an 1800 mm^{-1} grating for higher spectral resolution measurements. A grid of 8 × 8 $pixels^2$ with 50 μm spacing between points was employed for automated raster-scanning of the powder samples, with an acquisition time of 1 s and 5 accumulations at each measurement spot. Each set of data was then averaged over all 64 spectra of the raster scan.

Particle size distribution. The particle size distribution was measured with the Mastersizer 3000 from Malvern Panalytical GmbH according to ISO 13320 (01/2020). The device was validated every six months with reference materials. Median particle size was measured for pure ZrO_2 and V_2O_5 oxides and after ZrO_2 and V_2O_5 reagents were mixed at a Zr : V = 1 : 2 molar ratio and ground in a planetary ball for 10, 40, 90, 120 and 180 minutes. Further information on sample preparation and measurement procedure can be found in ESI.†

Computational simulations

In addition to experimental work, we performed *ab initio* computations. Structure optimisation and vibrational properties were computed using Density Functional Theory (DFT) with the Perdew–Burke–Ernzerhof (PBEsol) exchange–correlation functional[36] for solids as implemented in the Vienna ab initio simulation package (VASP).[37–40] Our calculations used the projected augmented-wave method[40,41] with a kinetic energy cut-off of 520 eV. We computed Raman-active modes with Phonopy[42,43] at the Gamma point by analysing the irreducible representations. Computational data was compared with experimental results. The *ab initio* spectra of phase-pure materials are based on ideal crystal structures and are therefore, unaffected by additional phases or instrumental errors. The simulated spectra can be used as a reference and to interpret the experimental spectra. More details on structure optimisation, vibrational properties computations and extraction of Raman-active modes are provided in the ESI,† computational simulations section.

Results and discussion

Solid state synthesis

Short calcination time. Calcination time is the first important parameter to consider in the case of solid-state reactions.

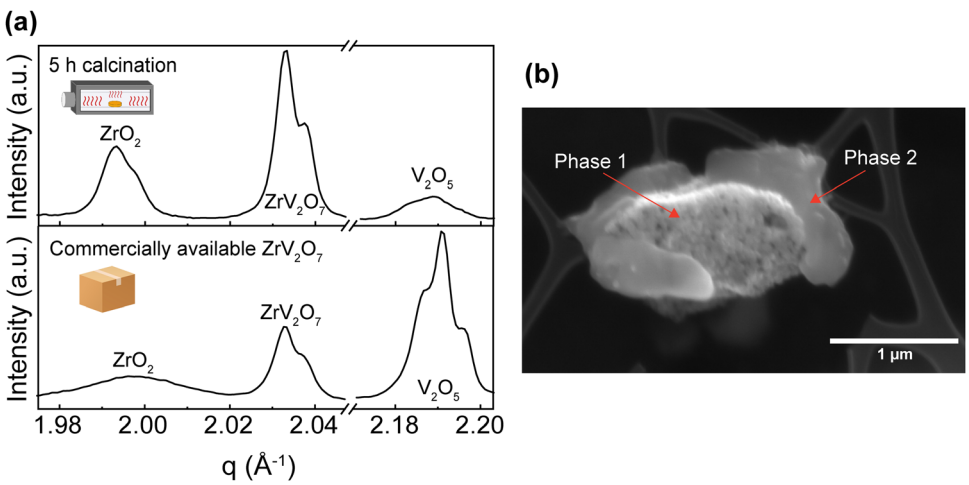

Fig. 2 (a) XRD of a solid-state 40′ 5 h multi-phase material and commercially available ZrV_2O_7 material. (b) SEM image (20 kV, SE) corresponds to the multi-phase solid-state 40′ 5 h material.

To confirm slow reaction kinetics and the presence of unreacted materials, we started with a short 5 h calcination step of 40-minute milled samples. Zirconium vanadate can be calcined at around 700 °C as its melting temperature is ~800 °C – a low temperature for ceramic materials.[17] Our investigation showed that after the reaction at 700 °C for 5 h, only 72.9% of ZrV_2O_7 was detected in the mixture. The remaining unreacted materials comprised 15.6% and 11.5% of V_2O_5 and ZrO_2, respectively (Fig. 2a). The non-uniform composition can be seen in the SEM images with two visibly different morphologies (Fig. 2b). In addition to synthesised samples analysis, we performed phase quantification on commercially available ZrV_2O_7 material (see Materials section). Although nominally available as zirconium vanadate, the material contains unreacted V_2O_5 and ZrO_2 along with an unidentified additional phase. Excluding this unknown component, the relative zirconium vanadate content (*i.e.*, among the identified phases) was barely 26.5%, whereas V_2O_5 was the main component at 56.6%. This suggests that commercially available ZrV_2O_7 was likely synthesised *via* a solid-state reaction with a short calcination step.

These experiments confirmed previous publications[17,44] in which short firing time was reported to affect purity and failed to provide a single-phase product. Our results highlight that a short, up to 10-hour calcination step at 700 °C failed to produce phase-pure ZrV_2O_7 from micrometre-sized starting powder. This is most likely caused by insufficient diffusion of elements, leading to a heterogeneous reaction throughout the sample. In contrast, some authors reported such an approach as successful and analysed electrical properties[23] and up-conversion luminescence[9] of the 2–8 h calcined material. In such cases, unreacted materials were not detected, however, no quantitative analysis was reported to confirm phase purity. It is worth noting that part of the reported XRD experimental data on ZrV_2O_7 is provided as JCPDS (Joint Committee on Powder Diffraction Standards) cards. This data, possibly, has been included as a part of modern databases (for example, Inorganic Crystal Structure Database (ICSD)), but the labels were changed in the process. Therefore, it is difficult to access said data and compare, determine or clarify phase purity.

Milling time. We proceeded with a 5 h calcination step to analyse the influence of the varying milling time on the purity of the final product and emphasize the importance of well-combined reagents. Increased milling time can reduce particle size and improve their distribution, resulting in enhanced reactivity, mixing and uniformity among the reactants. We used a planetary ball mill to combine ZrO_2 with V_2O_5, which is expected to be a more effective milling method than manual grinding in agate mortar. Before milling, ZrO_2 median particle size was $d_{50.3}$ = 1.808 μm and V_2O_5 $d_{50.3}$ = 1.412 μm. Particle size (volume) distribution was followed by milling oxides in a planetary ball mill for 10 min, 40 min, 1.5 h, 2 h, and 3 h. After 10 minutes of milling, the median particle size was 1.239 μm and remained similar (only a 1.29% decrease) after 40 minutes of milling. A more significant decrease of 17.6% to 1.008 μm was observed after 1.5 h milling. Further changes were gradual, with a decrease of around 3% every additional 30 minutes (Fig. 3 inset).

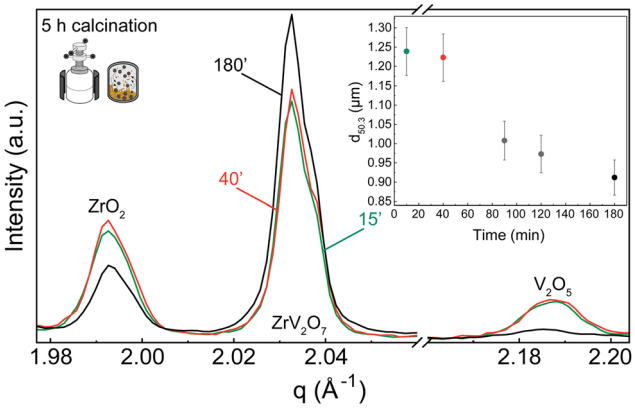

Fig. 3 XRD patterns of 15′, 40′, or 180′ milled precursors that were calcined for 5 h. The figure shows selected reflections corresponding to ZrO_2 (COD ID 9007485) and V_2O_5 (COD ID 9012221) phases diminishing with increasing milling time. Samples were heat treated for 5 h at 700 °C. Median particle size distribution after milling the ZrO_2 and V_2O_5 mixture in a planetary ball mill for 15′ (green), 40′ (red), 90′ (grey), 120′ (grey) and 180′ (black) (SD = 0.312 μm) are shown in the inset. Before the experiment, the ZrO_2 median particle size distribution was 1.808 μm and 1.412 μm for V_2O_5.

XRD patterns were collected for 15 min, 40 min, and 180 min milling experiments after 5 h calcination at 700 °C. All three samples contain residual phases of ZrO_2 and V_2O_5 because a shorter thermal treatment time was deliberately selected to demonstrate the importance of milling. The results correlate with the reduction in median particle size at around 1.5 h of milling. For 15 min and 40 min milled samples, the recorded XRD patterns are equivalent, and there is no clear improvement. However, increasing the milling time to 3 hours resulted in a decrease in unreacted oxides (Fig. 3). Following XRD patterns and particle size distribution, we can conclude that longer milling times reduce the particle size of reactants, improve reactivity, and create a more homogenous mixture, thus improving the quality of the final product.

In contrast to our approach, many published solid-state synthesis methods of ZrV_2O_7 and its substituted variations included combining ZrO_2 and V_2O_5 in an agate mortar.[4,9,10,13,20,22,23] Only Kul'bakin *et al.*[21] implemented a planetary mill to pre-disperse oxides – a more efficient tool than manual grinding. We report that increasing the milling time in the planetary ball mill to 180′ improved the purity of solid-state reaction products. However, it was insufficient to produce phase-pure materials, and further steps need to be taken. For further improvement, we considered two approaches: introducing calcination cycles by maintaining 40 or 180-minute milling of the reactants or implementing quenching techniques.

Repeated calcination. To improve the diffusion and elemental mixing, the calcination step of 20 h was repeated one, two, or three times with intermediate grinding. The amount of unreacted ZrO_2 and V_2O_5 phases slowly decreased with increasing number of calcination cycles (Fig. 4). According to the phase quantification of the 180′ milled sample that was calcinated three times for 20 h, the ZrV_2O_7 content reached 95.5%, with only 4.5% of ZrO_2 remaining.

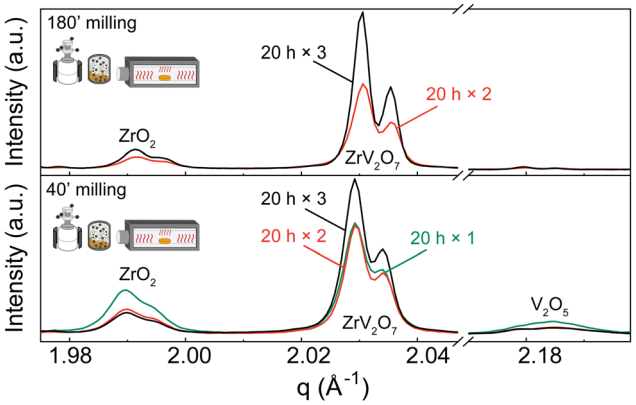

Fig. 4 XRD patterns of (a) 180′ and (b) 40′ milled samples calcined for 20 h one, two or three times with intermediate grindings in an agate mortar. Patterns show ZrO_2 and V_2O_5 phases diminishing with additional calcination cycles. Q shift occurs due to height misalignment during measurements. Systematic error is accounted for in Rietveld refinement. Refinement data for samples of interest is included in the ESI.† Experimental XRD patterns can be found at DOI: https://doi.org/10.5281/zenodo.12688634 (ref. 45) or upon request.

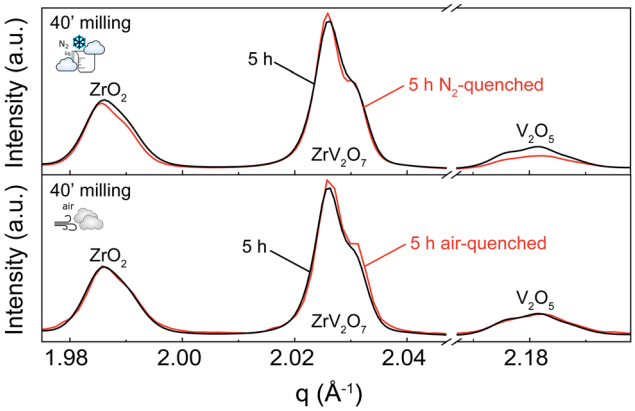

Fig. 5 XRD patterns comparing a 40′ 5 h sample quenched in liquid nitrogen *versus* a gradually cooled down 40′ 5 h sample (top) and an air-quenched 40′ 5 h sample *versus* the same 40′ 5 h sample (bottom).

We observed that during heat treatments V_2O_5 content was diminishing faster than ZrO_2, with only later remaining in the sample after three calcination cycles. Based on the thermogravimetric analysis (TGA) experiments described in the ESI† (Fig. S12), only a negligible amount of V_2O_5 could be lost during heat treatments due to a higher volatilization ratio of V_2O_5. Therefore, we hypothesize that different residual ratio is related to a more complex reaction mechanism that is beyond the scope of this work. For instance, as amorphous V_2O_5 can be obtained by ultrafast cooling from the melt,[46] such a process may occur in small amounts under slower cooling conditions. V_2O_5 remains present as an amorphous content that is untraceable in the XRD analysis, creating an apparent ZrO_2 excess. This is further discussed in the Quenching Experiments section. Alternatively, due to phase equilibrium conditions, there is a shift towards ZrO_2 phase formation.

While we cannot draw definite conclusions about residual ZrO_2, nonetheless, extended milling and repeated calcination with intermediate grinding provide sufficient elemental mixing and can produce a high-quality pure sample comparable with the ZrV_2O_7 synthesised *via* wet-chemical methods. With 95.5% zirconium vanadate purity and high crystallinity, we consider this sample suitable for further analysis and processing. We confirm that ZrO_2 and V_2O_5 solid-state reactions are very slow and thus require long processing times.[17]

Quenching experiments. In the second improvement approach, we performed a 40′ 5 h solid-state synthesis of ZrV_2O_7 with a quenching step. Air-quenching was compared with quenching in liquid nitrogen, and the purity of ZrV_2O_7 material was analysed. We followed a similar methodology to the already reported experiments, in which substituted $Zr_{0.70}V_{1.33}Mo_{0.67}O_{6.73}$ and $ZrV_{2-x}Mo_xO_{7+\delta}$ materials were synthesised.[10,22] Here, we define quenching as the fast-cooling process of a material in various fluids to obtain the phase-pure material. Direct exposure to air provides a moderate cooling rate, while immersion in liquid nitrogen offers a very rapid cooling due to the substantially lower liquid nitrogen temperature and its higher heat capacity.

A 5 h calcined sample was air-quenched from 700 °C to room temperature, and another 5 h calcined material was immersed in liquid nitrogen to achieve an extremely fast cooling effect. Quenching in liquid nitrogen showed an insignificant 3.5% reduction of unreacted materials compared to a slowly cooled-down sample. Subsequent phase quantification using Rietveld refinement revealed the composition to be 76.4% ZrV_2O_7, 13.4% V_2O_5, and 10.2% ZrO_2 (Fig. 5 top). Collected XRD patterns of air-quenched samples matched the ones of the corresponding slowly cooled-down counterparts. Thus, air-quenching proved insufficient to produce any observable difference (Fig. 5 bottom). According to our findings, quenching 5 h calcined ZrV_2O_7 in air or liquid nitrogen does not sufficiently improve sample purity and cannot replace repeated heating cycles and extended milling time. The synthesis of phase pure ZrV_2O_7 renders rigorous quenching protocols irrelevant.

While we consider the 3.5% total reduction of unreacted material insignificant, we observed different diminishing rates of V_2O_5 and ZrO_2. Quenching experiments in liquid nitrogen showed a reduction of V_2O_5 of 2.2% and only 1.3% of ZrO_2 compared with the 40′ 5 h sample. This information can further support the hypothesis that depending on processing conditions, V_2O_5, in addition to reaction with ZrO_2, can partially transition to its amorphous state, thus remaining present though untraceable in the XRD patterns.

The synthesis steps followed here were reported by Zhang *et al.*[22] and Wei *et al.*[10] They described 4 h calcination and quenching to obtain $Zr_{0.70}V_{1.33}Mo_{0.67}O_{6.73}$ and $ZrV_{2-x}Mo_xO_{7+\delta}$ materials. Zhang *et al.*[22] did not report any unreacted materials remaining in the sample. The investigation relied on energy dispersive spectroscopy (EDS), X-ray photoelectron spectroscopy (XPS), and XRD data to confirm the sample composition. The selected quenchant was not specified. Wei *et al.*[10] used cold water as a quenchant. They analysed the purity of the samples by refining powder XRD and synchrotron-radiation X-ray

diffraction (SXRD), indicating that the samples were pure. Possibly, the quenching step is a crucial requirement for compositions involving molybdenum (Mo) substitution.

In the case of elemental substitution with Mo, quenching techniques can be employed to enhance purity by preventing the exsolution and stabilising a specific desired phase. Additional elements, for example, Mo may lead to the formation and even stabilisation of undesired secondary phases; therefore, synthesis requires better control of phase formation. It is achieved by quenching a desired, possibly non-equilibrium state while preventing undesired, low-temperature processes, such as phase transformations, by slowing down the reaction kinetics. However, before considering substitution, it is crucial to know if quenching experiments can produce phase-pure material or if the problem of residual ZrO_2 and V_2O_5 phases would remain, creating a complex multi-phase system. If an additional quenching step does not improve the purity and produce multiphase material within the ZrV_2O_7 system, it remains true for a substituted material.

Solution-based synthesis methods

Hydrolytic and nonhydrolytic reactions were considered for our investigation of solution-based synthesis methods. We selected solvothermal, nonhydrolytic sol–gel hot injection methods (yielding sol–gel_160 °C and sol–gel_100 °C samples), ''classical'' hydrolytic sol- implementing Zr-alkoxide as a starting material (sol–gel_RO^-) and compared them with the already reported sol–gel method using NH_4VO_3 and $ZrOCl_2{\cdot}8H_2O$ as precursors (sol–gel_Cl).[26]

Phase quantification of all sol–gel synthesis products, except the hydrolytic (sol–gel_RO^-) reaction, pointed directly to a single-phase ZrV_2O_7. Sol–gel_RO^- showed a high purity of 97.1%, with only 2.9% of ZrO_2 detected. Phase quantification of the solvothermally prepared sample showed a detectable amount of ZrO_2 phase of 9.6% (Fig. 6a).

The morphology of the synthesis products mentioned above is shown in Fig. 6b. SEM images exhibit structures composed of dense particles that vary in size and form larger agglomerates. For sol–gel_160 °C, sol–gel_RO^-, sol–gel_Cl, and solvothermal reactions, the particles' size varies from <1 μm up to 10 μm and forms larger agglomerates reaching 60 μm in size (Fig. 6b, sol–gel_160 °C). The formation of smaller, more homogenous particles was observed for the nonhydrolytic (sol–gel_100 °C) and the hydrolytic (sol–gel_RO^-) reactions (Fig. 6b). Dominating $\sim$1–2 μm sized sphere-like shaped particles were observed. While both reactions yield smaller crystallites than other discussed methods, the sol–gel_RO^- reaction visibly provides the largest surface area.

The simple goal of improving Zr and V precursors mixing is driven by the sophisticated chemistry and physics of colloids. In the realm of hydrolytic synthesis, a common challenge arises from varying hydrolysis and condensation rates among different precursors (*i.e.*, those containing different metal centres).[31] They can affect elements' mixing in hydrolytic synthesis, potentially leading to inhomogeneous materials.[47,48] A phenomenon of phase separation may be effectively induced.[48,49] The addition

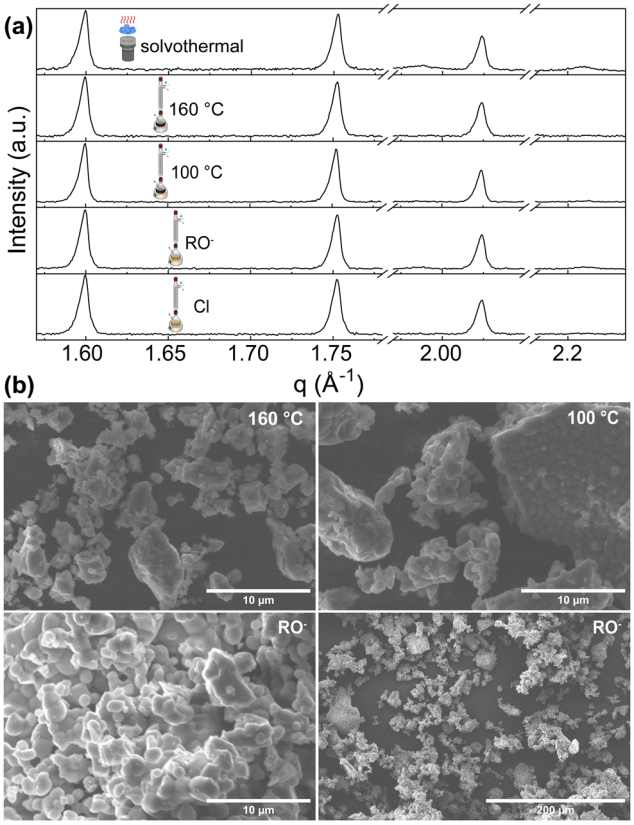

Fig. 6 (a) XRD patterns of ZrV_2O_7 from solution-based synthesis methods. Solvothermal synthesis results in a small amount of ZrO_2 phase. (b) SEM images of sol–gel_100 °C, sol–gel_160 °C and sol–gel_RO^- samples. The sol–gel_100 °C (b top right) and sol–gel_RO^- (b bottom) show smaller, more homogenous particles. The sol–gel_160 °C reaction image (top left) shows powder morphology, which is also similar to solvothermal and sol–gel_Cl reactions. SEM images of solvothermal and sol–gel_Cl reactions are provided in the ESI† Fig. S11.

of water can worsen the mixing effect, particularly in highly porous materials where the high surface tension of the water tends to cause the pores to shrink upon drying.[50] In contrast, operating under non-aqueous conditions offers improved control over solvolysis and polycondensation kinetics, thus enabling better homogeneity in the elemental mixing.[47,50] While the mechanistic details of solvolysis and condensation are beyond the scope of this work, they correlate with the phase composition of the final ZrV_2O_7.

According to our findings, both the non-hydrolytic sol–gel benzyl alcohol route and classical sol–gel approaches with varying reaction parameters were sufficient to produce high-purity samples. Hydrolysis rate control did not promote a more uniform mixing of elements. In addition to this, there was no significant difference in the phase composition (Fig. 6) when changing stirring time, reaction temperature, time, or reagents while implementing different synthesis routes. This may be due to an arbitrary threshold level of sufficient elemental mixing that ensures optimal results. All abovementioned solution-based reactions pass this threshold and modification of parameters does not show further improvement.

On the contrary, the solvothermal reaction showed the presence of an additional ZrO_2 phase. In the case of solvothermal reactions, we consider that the degree of phase separation depends not only on factors like the difference in precursor reactivities, their relative concentrations, and the solvent used but also on reaction conditions such as temperature and pressure. Even though solvolysis is significantly slower than hydrolysis, phase separation remains possible. When precursors show different reactivities towards the non-hydrolytic condensation reactions, the more reactive species can form a complex metal–organic cluster and phase separate before the less reactive one has a chance to condense into the network.[48,49] Such a mechanism could also be present in the case of the sol–gel reaction with alkoxide (sample, sol–gel_RO$^-$); small local alkoxide-based clusters can form and lead to the formation of a small amount of ZrO_2 during calcination.

An alternative explanation for the remaining ZrO_2 after the solvothermal reaction could indicate that pressure conditions and the elevated temperature led to partial dissolution and recrystallisation of zirconium compounds instead of hydrolysis and condensation reactions, leading to the formation of ZrV_2O_7.[29] Another possible consideration is that the reaction conditions could result in the initially formed ZrV_2O_7 decomposing to ZrO_2. Sakuntala *et al.*[51] reported pressure-induced decomposition at ambient temperatures. *In situ*, high-pressure Raman spectroscopic studies were carried out on ZrV_2O_7 samples synthesised *via* solid-state reaction. A potential shift in vanadium coordination was observed with applied pressure, transitioning from a fourfold coordination in ZrV_2O_7 to a fivefold in V_2O_5. In addition, Raman peaks corresponding to ZrO_2 were indicated to appear. These observations were assigned to ZrV_2O_7 decomposition. As increased temperatures can enhance such a process, we hypothesise that a lower pressure but elevated temperature of the solvothermal reaction could lead to partial decomposition and the presence of ZrO_2 (Fig. 6, solvothermal synthesis).

We indicate that sol–gel synthesis is a reliable method for obtaining high-purity samples. It also proved suitable for obtaining products with a desirable microstructure. However, elevated solvothermal reaction temperature and pressure conditions might lead to the formation of additional phases and provide lower-purity material.

Simulated and experimental Raman spectra comparison

As emphasized before, the phase composition and purity are crucial factors that allow for reproducible properties of the material. In this section, we provide a vivid illustration of this statement and show that ~70% or >30% purity ZrV_2O_7 powders yield different experimental results than phase-pure material. We compare Raman spectra from a solid-state reaction with 5 h calcination time (40' 5 h), commercially available zirconium vanadate and a sol–gel (sol–gel_100 °C) reaction product (Fig. 7). According to the previously discussed XRD data analysis, the commercially available sample mostly contained V_2O_5, while 40′ 5 h showed a mixture of phases with ~70% ZrV_2O_7 (Fig. 3). In contrast, the sol–gel_100 °C sample

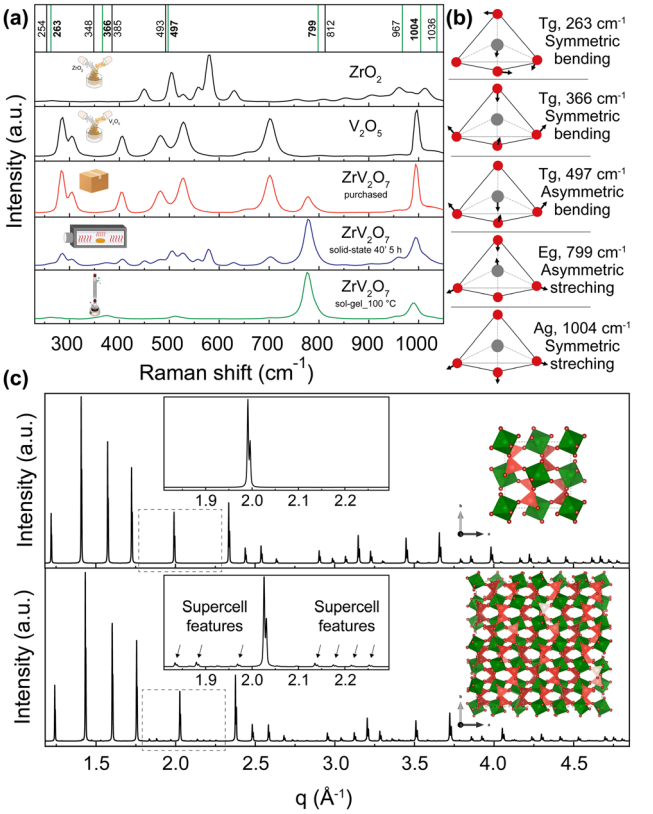

Fig. 7 (a) Raman spectra of ZrV_2O_7 synthesised *via* sol–gel (sol–gel_100 °C) route (green), 40′ 5 h solid-state reaction (blue) and purchased material (red). These spectra are compared with V_2O_5 and ZrO_2 reagents. The purchased material mostly matches V_2O_5 spectra, while the solid-state reaction product shows a combination of peaks representing both oxides and ZrV_2O_7. Vertical lines represent simulated Raman positions. Vibrations marked in green contribute to the Raman spectra and match the sol–gel reaction product within the margin of error. (b) Vibrations that correspond to 263, 366, 497, 799, and 1004 cm^{-1} frequencies are visualised above in a schematic way. Animations showing these vibrations are provided in the ESI.† (c) The XRD pattern of the ZrV_2O_7 structure used for computational simulations (c top) compared with the room temperature superstructure used in structure refinements (c bottom).

represents a phase-pure material (Fig. 6). As expected, analysis of Raman spectra revealed the abovementioned differences (Fig. 7). The commercially available sample mostly follows the vanadium oxide spectrum only with traces of ZrV_2O_7 appearing. Both commercially available and solid-state samples contain significant amounts of ZrO_2 and V_2O_5 oxides, deviating significantly from the desired material. On the contrary, the sol–gel sample shows only five main peaks that do not coincide with the spectra of residual phases. This could indicate and further confirm phase purity.

To interpret the Raman spectra and validate that our product is phase pure, we used *ab initio* simulated phonon data. The computational results are simulated for a defect-free and phase-pure material. A 40 atoms unit cell was used (Fig. 7c, top) because the actual low-temperature superstructure that includes 1080 atoms in the unit cell makes calculations computationally unfeasible (Fig. 7c, bottom). In the case of the supercell, *d* spacing between the planes is repeated, and we

see all higher-intensity ZrV_2O_7 peaks present in both structures. Only minor supercell features can be seen due to the slight tilting of ZrO_6 octahedra (green) and VO_4 tetrahedra (dark pink) (Fig. 7c, bottom). This shows that a smaller, 40 atoms cell, due to its structural similarity to the low-temperature ZrV_2O_7 phase, is suitable for obtaining computational Raman data.

First, we start with a quantitative comparison of experiment and simulation. We used a Voigt model to fit the experimental spectra. In addition, we carried out VASP and Phonopy *ab initio* computations to determine Raman active modes and corresponding Raman spectra peak positions. *Ab initio* values are marked in Fig. 7 as vertical lines. The frequency differences of the simulated and the matched fitted peak positions from the experiment are expressed as $\Delta\omega = |\omega_{fit} - \omega_{calc}|$. The comparison was performed for the peak positions that best matched the pattern. Some peaks were neglected as the peak intensities were too low for accurate fitting results. Differences vary from 0.8 cm^{-1} for the peak at 262 cm^{-1} and up to a maximum of 21 cm^{-1} for the peak at 778 cm^{-1}, considering the *ab initio* frequencies that best fit the experimental pattern. All the fitted peak positions and simulated frequencies are presented in the ESI,† Table S1. The differences were compared with the work of Bagheri and Komsa.[52] They simulated Raman spectra based on harmonic phonon computations *via* a high-throughput computation and compared it with experimental results. The reported examples showed that the most significant average difference for SiO_2 was 18.5 cm^{-1}, and the smallest deviation of 6 cm^{-1}. The deviations that occur in our work, therefore, correspond to expectations within the framework of the harmonic approximation and the level of theory (DFT with PBEsol functional). Further improvements could be achieved with the inclusion of additional anharmonic effects (*e.g.*, with temperature-dependent effective potentials[32] or other phonon renormalisation methods[34] or the quasi-harmonic approximation[42,53,54]). However, these methods have the disadvantage that they require additional computing time, which makes their implementation much more difficult than the harmonic approximation, especially for a compound such as ZrV_2O_7 with a rather large 40 atoms unit cell (Fig. 7). For this reason, they are not used here. Overall, the simulated results match the sol–gel_100 °C reaction experimental Raman spectra within the expected error from the level of theory and the harmonic nature of our approximation to the phonons computation. The largest deviation of 21 cm^{-1} corresponds to a 2.62% error. This discussed example is representative of all discussed sol–gel reactions and solid-state synthesis that can provide a high-purity ZrV_2O_7 phase through extended milling and calcination times.

We also further interpret the Raman spectra based on the computed phonons through visualisation of the vibrations. Vibrations corresponding to 263, 366, 497, 799, and 1004 cm^{-1} frequencies are shown in Fig. 7. Also, all of the animated computed vibrations are provided in the ESI.† Raman active frequencies mostly match the vibrations of vanadium and oxygen atoms within the VO_4 tetrahedra, except the 256 cm^{-1} frequency associated with Zr movements in ZrO_6 octahedra. Frequencies at 799 and 1036 cm^{-1} represent asymmetric, and 967 with 1004 cm^{-1} show symmetric stretching of VO_4 tetrahedra. With 799 and 1004 cm^{-1} vibrations contributing the most to the Raman spectra. Smaller intensity peaks at 263, 366, and 497 cm^{-1} correspond to symmetric and asymmetric bending of VO_4 tetrahedra, respectively. These simulated optically active modes of phase pure ZrV_2O_7 structure match the frequencies in the ZrV_2O_7 experimental Raman spectrum. In the case of multi-phase materials, due to peak overlap and complex peak assignment, structural information might be lost. In addition to this, validation with theoretical data would be impossible, thus preventing the detailed analysis of Raman active atom vibrations (*e.g.* by analysing the vibrational eigenvectors from the phonon computation as done in Fig. 7). Therefore, in this case, the necessity of a phase-pure material is further emphasised.

Hemamala *et al.*[55] also analysed Raman spectra of ZrV_2O_7 from experimental data and *ab initio* calculations. The authors implemented Perdew–Burke–Ernzerhof (PBE) functional[56] and (4 × 4 × 4) *k*-point sampling mesh. Force convergence of 0.001 eV $Å^{-1}$ for geometry relaxation was used, and 0.001 meV convergence for self-consistent force calculations. In contrast, we used PBEsol functional, a *Γ*-centre grid of (6 × 6 × 6) *k*-points; $\Delta E < 10^{-8}$ and $\Delta E < 10^{-6}$ eV for the electronic and structural optimisation, respectively, thus increasing computational accuracy. Reported Raman-active modes centred at 263, 280, 367, 380, 404, 511, 774, 957, 984, and 1023 cm^{-1} confirm our results. Similar to our study, authors assigned lower frequency modes to the symmetric VO_4 tetrahedra bending, 404 and 511 cm^{-1} to the asymmetric bending, and 774 cm^{-1} to the asymmetric stretching. High-frequency modes were assigned to the symmetric stretching of VO_4 tetrahedra.

Thermal expansion of multi-phase materials

In this section, we discuss how the phase purity correlates with and affects the NTE property of the materials. Zirconium vanadate garnered interest due to its anomalous isotropic negative thermal expansion behaviour. Negative thermal expansion is a very rare property. Thus, it is very unlikely that secondary phases besides ZrV_2O_7 in a non-phase-pure product would share such an attribute. In the case of ZrV_2O_7, many synthesised and even commercially available materials contain unreacted precursors – zirconium and vanadium oxides. As temperature changes, we will inevitably see structural differences between zirconium vanadate and unreacted materials. This directly influences the negative thermal expansion property of a material. For example, in Fig. 8, for the peaks representing ZrO_2 and V_2O_5 phases, when the temperature is increased, we see a decrease in q (where $q = 2\pi/d$). This means that d spacing increases, and we observe ordinary unit cell expansion. In the case of ZrV_2O_7, we see the opposite extraordinary effect of unit cell contraction (Fig. 8). This crucial difference within multi-phase materials prevents the evaluation of the fundamental crystallographic principles of negative thermal expansion. Thus, the presence of additional phases would affect any applicational implementation of ZrV_2O_7 relying on NTE.

All implemented characterisation methods, such as XRD, SEM and Raman spectroscopy, revealed differences between

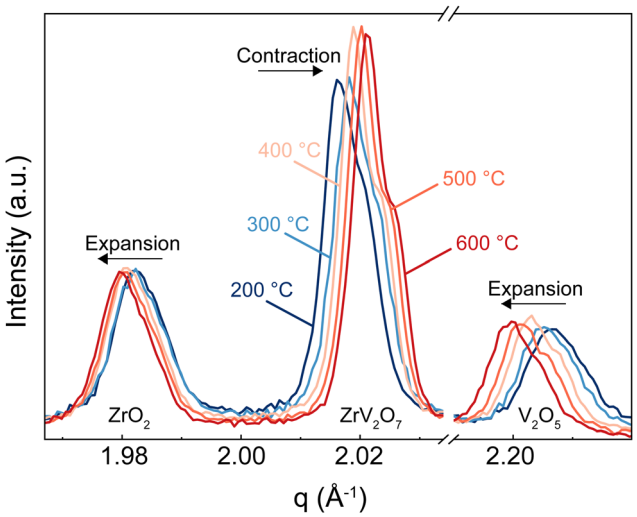

Fig. 8 *In situ* XRD characterisation of ZrV_2O_7 sample synthesised *via* solid-state synthesis and calcined for 5 h at 700 °C. The peak corresponding to ZrV_2O_7 shows unit cell contraction in the 200–500 °C range, while residual ZrO_2 and V_2O_5 phases display opposite unit cell expansion behaviour.

phase-pure and multiphase materials. Multiphase materials lead to reproducibility issues and difficulty in material characterisation. This is also true if substitution is considered, as it increases the probability of the final local composition diverging and leading to the formation of additional competing phases. Due to the cubic crystal structure, the unit cell of zirconium vanadate contracts isotropically with temperature.[4] At the same time, common residual ZrO_2 and V_2O_5 phases show the usual positive thermal expansion. V_2O_5 adopts an orthorhombic crystal system and ZrO_2 a monoclinic one, both showing highly anisotropic behaviour, making it challenging to assess discrepancies in the experimental data. This could create issues in dilatometry measurements. Another commonly applied method is the energy dispersive X-ray (EDX) analysis, but this reveals only the presence of elements and does not allow differentiation between residual ZrO_2 and V_2O_5 phases and ZrV_2O_7. On the contrary, high-temperature XRD analysis shows clear differences in unit cell expansion between ZrV_2O_7 and remaining oxides. It is a compelling technique to confirm the purity of negative thermal expansion materials or detect phases showing positive thermal expansion. However, data processing remains more challenging in comparison to phase-pure materials.

Conclusions

The synthesis of pure, homogeneous materials is essential for comprehensive material characterisation. Our study shows that the solid-state synthesis of ZrV_2O_7 requires careful consideration of various processing parameters to achieve high purity.

Initial attempts using a 1 to 5 hours calcination step yielded multiphase materials containing only ~70% ZrV_2O_7. However, by optimising the milling time and implementing repeated calcination cycles with intermediate grinding, we successfully produced a 95.5% pure ZrV_2O_7 sample.

We also investigated alternative wet chemical methods, including sol–gel and solvothermal synthesis. While solvothermal reactions resulted in the formation of an additional ZrO_2 phase due to elevated temperature and pressure conditions, sol–gel methods proved highly effective in producing single-phase zirconium vanadate samples.

Raman spectroscopy was used as a powerful tool to assess sample purity. Spectra from multiphase materials showed peaks from unreacted precursors, making meaningful interpretation difficult. In contrast, Raman data from phase-pure samples agreed well with *ab initio* simulated phonon data, falling within the expected error range of density functional theory calculations within the harmonic approximation. This agreement allowed detailed analysis and visualisation of lattice vibrations, further confirming material purity.

In addition, high-temperature XRD proved to be invaluable in distinguishing between unreacted materials and the desired ZrV_2O_7 phase, revealing their contrasting thermal expansion behaviour. This technique is critical for verifying sample composition and purity.

In conclusion, our study highlights the importance of meticulous synthesis procedures and comprehensive characterisation techniques in the preparation and confirmation of high-purity ZrV_2O_7. These results not only advance our understanding of this specific material but also provide valuable insights for the broader field of materials science, highlighting the critical interplay between synthesis methods, characterisation techniques and material properties.

Author contributions

Conceptualization (BM, TMS, JG, AM). Investigation (performing the experiments (AM, BM)), data/evidence collection (MZ collected Raman spectra; AM, TMS, SK, ME conducted synchrotron experiments; JB and AM conducted the theoretical calculations; AM performed XRD and TGA experiments; TMS, AM and SK collected high-temperature XRD). Formal analysis (JB, JG, and AM analysed theoretical computations; AM and TMS performed Raman, TGA, and XRD data analysis; AM analysed SEM and particle size distribution data). Supervision (TMS, BM, JG). Visualization (AM, SK, ME). Writing (original draft (AM); review & editing (all authors contributed to the manuscript)).

Data availability

The complete dataset is published on Zenodo (DOI: **https://doi.org/10.5281/zenodo.12688634**).[45] Any other raw data are available from the corresponding authors upon reasonable request.

Conflicts of interest

There are no conflicts to declare.

Acknowledgements

We acknowledge DESY (Hamburg, Germany), a member of the Helmholtz Association HGF, for providing experimental facilities. Parts of this research were carried out at PETRA III, and we would like to thank Dr Alba San Jose Mendez for assistance in using P02.1 Powder Diffraction and Total Scattering Beamline. Beamtime was allocated for proposal I-20230110. We would also like to thank Franziska Lindemann for particle size distribution measurements and Michaela Lagleder for assistance in SEM imaging performed at the electron microscopy centre, Federal Institute for Materials Research and Testing (Berlin, Germany). AM, JB and JG would like to acknowledge the Gauss Centre for Supercomputing e.V. (**https://www.gauss-centre.eu**) for funding the DFT-related work by providing generous computing time on the GCS Supercomputer SuperMUC-NG at Leibniz Supercomputing Centre (**https://www.lrz.de**) (Project pn73da).

References

1 Q. Li, *et al.*, Chemical Diversity for Tailoring Negative Thermal Expansion, *Chem. Rev.*, 2022, **122**, 8438–8486.
2 K. Takenaka, Giant Negative Thermal Expansion Materials: Progress of Research and Future Prospects, *Mater. Trans.*, 2024, **65**, 243–252.
3 R. L. Withers, J. S. O. Evans, J. Hanson and A. W. Sleight, An in situ temperature-dependent electron and X-ray diffraction study of structural phase transitions in ZrV_2O_7, *J. Solid State Chem.*, 1998, **137**, 161–167.
4 V. Korthuis, *et al.*, Negative Thermal Expansion and Phase Transitions in the $ZrV_{2-x}P_xO_7$ Series, *Chem. Mater.*, 1995, **7**, 412–417.
5 J. S. O. Evans, Negative thermal expansion materials, *J. Chem. Soc., Dalton Trans.*, 1999, **0**, 3317–3326.
6 Q. Liu, *et al.*, Structural, negative thermal expansion and photocatalytic properties of ZrV_2O_7: a comparative study between fibers and powders, *Mater. Charact.*, 2014, **96**, 63–70.
7 L. Shreenivasa, *et al.*, Engineering of highly conductive and mesoporous ZrV_2O_7: a cathode material for lithium secondary batteries, *J. Solid State Electrochem.*, 2019, **23**, 1201–1209.
8 P. P. Sahoo, S. Sumithra, G. Madras and T. N. Guru Row, Synthesis, Structure, Negative Thermal Expansion, and Photocatalytic Property of Mo Doped ZrV_2O_7, *Inorg. Chem.*, 2011, **50**, 8774–8781.
9 J. Wang, *et al.* Temperature-controlled Upconversion Luminescence of Yb^{3+}/Er^{3+} Co-doped ZrV_2O_7 Crystals, *Asia Communications and Photonics Conference T4A.151* (Optica Publishing Group, Asia Communications and Photonics Conference, 2021), DOI: **10.1364/ACPC.2021.T4A.151**.
10 W. Wei, *et al.*, Realizing isotropic negative thermal expansion covering room temperature by breaking the superstructure of ZrV_2O_7, *Appl. Phys. Lett.*, 2020, **116**, 181902.
11 Q. Liu, *et al.*, Influence of W doped ZrV_2O_7 on structure, negative thermal expansion property and photocatalytic performance, *Appl. Surf. Sci.*, 2014, **313**, 41–47.
12 B. Yuan, *et al.*, Low thermal expansion over a wide temperature range of $Zr_{1-x}Fe_xV_{2-x}Mo_xO_7$ ($0 \leq x \leq 0.9$), *Mater. Chem. Phys.*, 2016, **170**, 162–167.
13 B.-H. Yuan, *et al.*, High Solubility of Hetero-Valence Ion (Cu^{2+}) for Reducing Phase Transition and Thermal Expansion of $ZrV_{1.6}P_{0.4}O_7$, *Chin. Phys. Lett.*, 2014, **31**, 076501.
14 I. Yanase, T. Kojima and H. Kobayashi, Effects of Nb and Y substitution on negative thermal expansion of $ZrV_{2-X}P_XO_7$ ($0 \leqq X \leqq 0.8$), *Solid State Commun.*, 2011, **151**, 595–598.
15 J. S. O. Evans, J. C. Hanson and A. W. Sleight, Room-Temperature Superstructure of ZrV_2O_7, *Acta Crystallogr., Sect. B: Struct. Sci.*, 1998, **54**, 705–713.
16 O. Yu Khyzhun, V. L. Bekenev, M. V. Karpets and I. Yu Zavaliy, First-principles FP-LAPW calculations and X-ray spectroscopy studies of the electronic structure of Zr_3V_3O and $Zr_3V_3O_{0.6}$ oxides, *J. Phys. Chem. Solids*, 2012, **73**, 1302–1308.
17 R. C. Buchanan and G. W. Wolter, Properties of Hot-Pressed Zirconium Pyrovanadate Ceramics, *J. Electrochem. Soc.*, 1983, **130**, 1905.
18 N. Khosrovani, A. W. Sleight and T. Vogt, Structure of ZrV_2O_7 from −263 to 470 °C, *J. Solid State Chem.*, 1997, **132**, 355–360.
19 S. Carlson and A. Andersen, High-pressure properties of TiP_2O_7, ZrP_2O_7 and ZrV_2O_7, *J. Appl. Crystallogr.*, 2001, **34**, 7–12.
20 T. Hisashige, T. Yamaguchi, T. Tsuji and Y. Yamamura, Phase Transition of $Zr_{1-x}Hf_xV_2O_7$ Solid Solutions Having Negative Thermal Expansion, *J. Ceram. Soc. Jpn.*, 2006, **114**, 607–611.
21 I. Kul'bakin, S. Fedorov, A. Vorob'ev and V. Belousov, Transport properties of ZrV_2O_7–V_2O_5 composites with liquid – channel grain boundary structure, *Russ. J. Electrochem.*, 2013, **49**, 878–882.
22 M. Zhang, *et al.*, A novel negative thermal expansion material of $Zr_{0.70}V_{1.33}Mo_{0.67}O_{6.73}$, *RSC Adv.*, 2017, **7**, 3934–3940.
23 B. Yuan, *et al.*, Electrical properties and dielectric relaxation behavior of zirconium vanadate, *Ceram. Int.*, 2018, **44**, 21621–21625.
24 M. F. Elkady, M. A. Alrafaa and N. A. El Essawy, Morphological and electrical properties of zirconium vanadate doped with cesium, *Beni-Suef Univ. J. Basic Appl. Sci.*, 2014, **3**, 229–237.
25 Q. Liu, X. Cheng, X. Sun, J.-Y. Yang and H. Li, Synthesis and characterization of sol–gel derived ZrV_2O_7 fibers with negative thermal expansion property, *J. Sol-Gel Sci. Technol.*, 2014, **72**, 502–510.
26 I. Yanase, H. Chida and H. Kobayashi, Fabrication and negative thermal expansion properties of P-substituted ZrV_2O_7 sintered bodies, *J. Eur. Ceram. Soc.*, 2018, **38**, 221–226.
27 Q. Kuang, Y. Zhao, Y. Dong and Q. Fan, Sol–gel synthesized zirconium pyrovanadate as a high-capacity cathode for rechargeable Li batteries, *Electrochim. Acta*, 2015, **170**, 229–233.
28 Q. Li, *et al.*, Superstructure ZrV_2O_7 nanofibres: thermal expansion, electronic and lithium storage properties, *Phys. Chem. Chem. Phys.*, 2016, **18**, 32160–32168.

29 G. Demazeau, Solvothermal reactions: an original route for the synthesis of novel materials, *J. Mater. Sci.*, 2008, **43**, 2104–2114.
30 A. Vioux and P. Hubert Mutin, Nonhydrolytic Sol–Gel Technology, in L. Klein, M. Aparicio and A. Jitianu (ed.), *Handbook of sol–gel Science and Technology*, Springer International Publishing, Cham, 2016, pp. 1–27, DOI: 10.1007/978-3-319-19454-7_28-1.
31 A. E. Danks, S. R. Hall and Z. Schnepp, The evolution of 'sol–gel' chemistry as a technique for materials synthesis, *Mater. Horiz.*, 2016, **3**, 91–112.
32 O. Hellman, I. A. Abrikosov and S. I. Simak, Lattice dynamics of anharmonic solids from first principles, *Phys. Rev. B: Condens. Matter Mater. Phys.*, 2011, **84**, 180301.
33 Z. Zhu, J. Park, H. Sahasrabuddhe, A. M. Ganose, R. Chang, J. W. Lawson and A. Jain, A high-throughput framework for lattice dynamics, *npj Comput. Mater.*, 2024, **10**, 258.
34 F. Eriksson, E. Fransson and P. Erhart, The Hiphive Package for the Extraction of High-Order Force Constants by Machine Learning, *Adv. Theory Simul.*, 2019, **2**, 1800184.
35 M. Niederberger and G. Garnweitner, Organic reaction pathways in the nonaqueous synthesis of metal oxide nanoparticles, *Chem. Weinh. Bergstr. Ger*, 2006, **12**, 7282–7302.
36 J. P. Perdew, *et al.*, Restoring the Density-Gradient Expansion for Exchange in Solids and Surfaces, *Phys. Rev. Lett.*, 2008, **100**, 136406.
37 G. Kresse and J. Hafner, Ab initio molecular dynamics for liquid metals, *Phys. Rev. B: Condens. Matter Mater. Phys.*, 1993, **47**, 558–561.
38 G. Kresse, J. Furthmüller and J. Hafner, Theory of the crystal structures of selenium and tellurium: the effect of generalized-gradient corrections to the local-density approximation, *Phys. Rev. B: Condens. Matter Mater. Phys.*, 1994, **50**, 13181–13185.
39 G. Kresse and J. Furthmüller, Efficient iterative schemes for ab initio total-energy calculations using a plane-wave basis set, *Phys. Rev. B: Condens. Matter Mater. Phys.*, 1996, **54**, 11169–11186.
40 G. Kresse and D. Joubert, From ultrasoft pseudopotentials to the projector augmented-wave method, *Phys. Rev. B: Condens. Matter Mater. Phys.*, 1999, **59**, 1758–1775.
41 P. E. Blöchl, Projector augmented-wave method, *Phys. Rev. B: Condens. Matter Mater. Phys.*, 1994, **50**, 17953–17979.
42 A. Togo, First-principles Phonon Calculations with Phonopy and Phono3py, *J. Phys. Soc. Jpn.*, 2023, **92**, 012001.
43 A. Togo, L. Chaput, T. Tadano and I. Tanaka, Implementation strategies in phonopy and phono3py, *J. Phys.: Condens. Matter*, 2023, **35**, 353001.
44 V. Cirilli, A. Burdese and C. Brisi, La corrosione di leghe refrattarie da parte di ceneri di petrolio contenenti vanadio, *Atti Della R. Accad. Delle Sci. Torino*, 1961, **95**, 399–424.
45 A. Miliūtė, *et al.*, Synthesis and phase purity of the negative thermal expansion material ZrV2O7, 2024, DOI: 10.5281/zenodo.12688634.
46 M. Nabavi, C. Sanchez and J. Livage, Structure and properties of amorphous V_2O_5, *Philos. Mag. B*, 1991, **63**, 941–953.
47 A. Styskalik, D. Skoda, C. E. Barnes and J. Pinkas, The Power of Non-Hydrolytic Sol–Gel Chemistry: A Review, *Catalysts*, 2017, **7**, 168.
48 T. M. Stawski, *et al.*, Nanostructure Development in Alkoxide-Carboxylate-Derived Precursor Films of Barium Titanate, *J. Phys. Chem. C*, 2012, **116**, 425–434.
49 T. M. Stawski, *et al.*, Development of Nanoscale Inhomogeneities during Drying of Sol–Gel Derived Amorphous Lead Zirconate Titanate Precursor Thin Films, *Langmuir*, 2011, **27**, 11081–11089.
50 V. Smeets, A. Styskalik and D. P. Debecker, Non-hydrolytic sol–gel as a versatile route for the preparation of hybrid heterogeneous catalysts, *J. Sol-Gel Sci. Technol.*, 2021, **97**, 505–522.
51 T. Sakuntala, *et al.*, Pressure-induced amorphization and decomposition in ZrV_2O_7: a Raman spectroscopic study, *Phys. Rev. B: Condens. Matter Mater. Phys.*, 2007, **75**, 174119.
52 M. Bagheri and H.-P. Komsa, High-throughput computation of Raman spectra from first principles, *Sci. Data*, 2023, **10**, 80.
53 A. Togo and I. Tanaka, First principles phonon calculations in materials science, *Scr. Mater.*, 2015, **108**, 1–5.
54 R. P. Stoffel, C. Wessel, M.-W. Lumey and R. Dronskowski, Ab Initio Thermochemistry of Solid-State Materials, *Angew. Chem., Int. Ed.*, 2010, **49**, 5242–5266.
55 U. L. C. Hemamala, *et al.*, High-pressure Raman and infrared study of ZrV_2O_7, *Solid State Commun.*, 2007, **141**, 680–684.
56 J. P. Perdew, K. Burke and M. Ernzerhof, Generalized Gradient Approximation Made Simple, *Phys. Rev. Lett.*, 1996, **77**, 3865–3868.

